

X-RAY FLUORESCENCE FROM SUPER-EDDINGTON ACCRETING BLACK HOLES

LARS LUND THOMSEN,^{1,2} JANE LIXIN DAI,^{1,2} ENRICO RAMIREZ-RUIZ,^{3,2} ERIN KARA,⁴ AND CHRIS REYNOLDS⁵

¹*Department of Physics, University of Hong Kong, Pokfulam Road, Hong Kong*

²*DARK, Niels Bohr Institute, University of Copenhagen, Lyngbyvej 2, 4. floor, 2100 Copenhagen Ø, Denmark*

³*Department of Astronomy and Astrophysics, University of California Santa Cruz, 1156 High Street, Santa Cruz, CA 95060, USA*

⁴*MIT Kavli Institute for Astrophysics and Space Research Massachusetts Institute of Technology 77 Massachusetts Avenue, 37-241 Cambridge, MA 02139*

⁵*Institute of Astronomy, University of Cambridge, Cambridge, CB3 0HA, UK*

ABSTRACT

X-ray reverberation has proven to be a powerful tool capable of probing the innermost region of accretion disks around compact objects. Current theoretical effort generally assumes that the disk is geometrically thin, optically thick and orbiting with Keplerian speed. Thus, these models cannot be applied to systems where super-Eddington accretion happens because the thin disk approximation fails in this accretion regime. Furthermore, state-of-the-art numerical simulations show that optically thick winds are launched from super-Eddington accretion disks, and thereby changing the reflection geometry significantly from the thin disk picture. We carry out theoretical investigations on this topic by focusing on the Fe K α fluorescent lines produced from super-Eddington disks, and show that their profiles are shaped by the funnel geometry and wind acceleration. We also systematically compare the Fe line profiles from super-Eddington thick disks to those from thin disks, and find that the former are substantially more blueshifted and symmetric in shape. Therefore, careful analysis of the Fe K α line profile can be used to identify systems undergoing super-Eddington accretion.

Keywords: accretion, accretion disks — black hole physics — line: profiles — magnetohydrodynamics (MHD)

arXiv:1907.11462v1 [astro-ph.GA] 26 Jul 2019

1. INTRODUCTION

Some of the most luminous astrophysical sources, such as the active galactic nuclei (AGNs), X-ray binaries and long gamma-ray bursts, are all powered by the accretion of gas onto black holes (BHs). The viscous or magnetic process in the gaseous disk or torus transports angular momentum outwards and also heats up the disk (Shakura & Sunyaev 1973; Balbus & Hawley 1991). In this process, part of the mass-energy of the gas is effectively converted into energy and released in the form of radiation or large-scale outflows in the wind and jet regions. Therefore, it is of the uttermost importance to study the detailed structure of accretion disks. While a thin disk rotating at Keplerian speed with no outflows (Shakura & Sunyaev 1973; Novikov & Thorne 1973) is widely applied to explain many accreting systems, this disk model will break down when the accretion rate is very low or very high. For the latter case, it is because there exist a theoretical upper threshold of radiation level called the Eddington limit, which corresponds to the equilibrium where the radiation pressure force on a gas element balances the gravitational force from the BH. The Eddington luminosity L_{Edd} and the corresponding Eddington accretion rate \dot{M}_{Edd} are given by the following equations

$$L_{\text{Edd}} \approx 1.26 \times 10^{38} \left(\frac{M}{M_{\odot}} \right) \text{ erg s}^{-1} \quad \text{and} \quad \dot{M}_{\text{Edd}} = \frac{L_{\text{Edd}}}{\eta c^2}, \quad (1)$$

where M/M_{\odot} is the mass of the central object in the unit of solar mass M_{\odot} , c is the speed of light, and η is called the radiative efficiency. When the accretion level exceeds this limit, the radiation pressure will become large enough to change the disk structure making it geometrically thick (Begelman 1978; Abramowicz et al. 1980). Recently, great progress has also been achieved through numerical studies with the aid of general relativistic radiation magnetohydrodynamic (GRRMHD) codes (Ohsuga et al. 2009; Jiang et al. 2014; McKinney et al. 2014; Sądowski et al. 2014; Dai et al. 2018), which have shown that the Eddington luminosity limit can be broken and large-scale optically-thick winds are launched from the geometrically thick disk. This has significant implications on how much mass can eventually be accreted onto the BH, how much energy is carried away by wind and how the radiative output is affected by the wind-launching. Fast winds, consistent with theoretical results, have also been observed from ultra-luminous X-ray sources (ULXs) (e.g., Pinto et al. 2016) and tidal disruption events (e.g., Kara et al. 2016, 2018; Alexander et al. 2017), which both likely undergo super-Eddington accretion.

Tremendous effort has been put into understanding the structures of accretion disks. In particular, X-ray reverberation, first proposed by Fabian et al. (1989), has proved to be very useful in giving direct measurement of the inner disk geometry by combing both the spectral and temporal information from this region. As presented in the review by Reynolds (2014), the classical approach to X-ray reverberation is to have a hot and compact corona, which produces non-thermal X-rays, located above the cold accretion disk. The cold disk is therefore illuminated by the corona emission, which gives rise to an X-ray reflection spectrum. One notable feature of the reflection spectrum is the Fe $K\alpha$ fluorescent lines produced from the ionization of the illuminated disk (Matt et al. 1993). Here, GR and Doppler effects between the rotating disk and the observer will produce broadened and skewed fluorescent line profiles. This theoretical model has been successfully applied to constrain the spin of BHs in systems where the disk has a razor thin structure rotating with relativistic Keplerian speed (e.g., Fabian et al. 1989; Reynolds & Begelman 1997; Reynolds et al. 1999; Reynolds 2014). The line profile has a dependence on the BH spin because the innermost edge of a thin disk is given by the innermost stable circular orbit (ISCO) of the BH, which is smaller for a BH with larger prograde spin. X-ray reverberation has also been used to study the nature of corona formation, which we still do not fully understand (Blandford et al. 2017; Yuan et al. 2019). Therefore, various corona geometries have been investigated. The simplest and best-studied geometry is the ‘‘lamppost’’ model, where the corona is assumed to be an isotropically-radiating point source located at a few R_g above the BH (Matt et al. 1991; Reynolds & Begelman 1997; Reis & Miller 2013). Other corona geometries that have been investigated include an off-axis compact corona or an extended corona (see Wilkins & Fabian 2012). Corona with geometry changing on short timescales, which is associated with changes in accretion state, has also been reported recently (Kara et al. 2019).

While most of the effort, which is described above, assumes a thin Keplerian disk structure, recently, efforts have also been made in trying to incorporate finite disk thickness from analytical disk models (Wu & Wang 2007; Taylor & Reynolds 2018) or realistic structures from thin disk simulations (e.g., Schnittman et al. 2013). However, previous theoretical investigation on X-ray reverberation has not covered accretion flow with optically-thick winds, which can be formed when a disk undergoes super-Eddington accretion. One will expect the X-ray reverberation signatures from super-Eddington disks to be very different to those arising from thin disks, since the corona emission will no longer be reprocessed by the surface of the (thin) disk but by the optically thick winds. One will also expect the trajectories of the reflected photons and their redshift to be different due to the geometry and the motion of the optically thick winds as compared to the usually assumed equatorial Keplerian flow. One main reason for the lack of literature on this topic is that the structure of super-Eddington accretion flow has only recently been resolved by simulations. Another reason is that observational signatures of X-ray reverberation from a definitively super-Eddington accretion flow has not been reported until recently in Kara et al. (2016), where the strong blueshift of the Fe line and

its lag have been observed from the jetted TDE *Swift* J1644. In order to successfully explain the salient observational features, the authors also conducted preliminary theoretical modeling of the Fe line by assuming the funnel produced in super-Eddington accretion flow has a conical shape.

As a first step towards better understanding X-ray reverberation from super-Eddington accretion flows and motivated by the framework described in Kara et al. (2016), we study the fluorescent Fe $K\alpha$ emission line profiles derived from state-of-the-art disk simulations. We study in details the profile of a super-Eddington disk previously simulated in Dai et al. (2018) and calculate the corona emission reflection surface, which is embedded in the optically thick winds, and its ionization level (Section 2). Due to the wind region having a lower density than dense disks, the ionization level of the reflection surface is naturally higher, so fluorescent Fe $K\alpha$ lines with a higher rest-frame energy are expected to be produced. Next, we apply GR ray-tracing techniques to trace the corona photons reflected by this surface to an observer, and we calculate the theoretical Fe $K\alpha$ line profile and check its dependence on various parameters such as the inclination angle and corona location (Section 3). Furthermore, we do a systematic comparison of the Fe $K\alpha$ line profiles between those produced from the simulated super-Eddington accretion disk and those produced from standard thin disks (Section 4). We show that a typical Fe $K\alpha$ line from super-Eddington disks exhibits a large blueshift, while the thin disk counterparts are either dominated by redshift or show much lower blueshift depending on the inclination angle. Also, the line profiles from super-Eddington disks are more symmetric with respect to the line center. Therefore, these morphological differences of the Fe $K\alpha$ line can effectively serve as indicators of super-Eddington accretion. Lastly, we discuss the implications and future directions of this work (Section 5).

2. DISK PROFILE, FUNNEL GEOMETRY AND IONIZATION LEVEL

First, let us briefly summarize the basic and relevant properties for X-ray reverberation on a super-Eddington accretion disk structure. In order to do this, we have set the super-Eddington disk profile simulated in Dai et al. (2018) in a classical X-ray reflection picture, and we present it in Fig. 1 along with an illustration of the corona, disk, wind and funnel structures. The disk surrounds a supermassive BH with mass of $5 \times 10^6 M_\odot$ and a fast spin parameter of 0.8. We calculate the time and azimuthal-averaged profile of the disk after the inflow equilibrium has been established to $r \approx 100 R_g$ ($R_g = GM_{\text{BH}}/c^2$ is the gravitational radius of the BH, with G being the gravitational constant and M_{BH} being the BH mass). The averaged accretion rate is about $15 \dot{M}_{\text{Edd}}$ during this phase. One can also notice that consistent with theoretical predictions, the inner edge of the thick disk gets much closer to the BH than the ISCO, since the disk is supported by radiation pressure. A relativistic jet is launched magnetically due to the large-scale magnetic flux threading the inner disk region. Winds, which are denser and slower towards the equator, are also launched from the thick accretion disk, thus creating an optically-thin “funnel” near the pole. The emission of the corona can be reflected by and irradiate the wall of the funnel. Here, we adopt the standard lamppost model and place a hard X-ray emitting compact corona at a height of $h_{\text{LP}} = \text{few} \times R_g$. (Note that the corona is placed artificially as no self-consistent accretion disk simulations exists yet that can simulate the formation of a compact corona.) We also cut out the jet region (where the gas pressure over the magnetic pressure $\beta \approx 1$) since the gas density in the jet can be numerically boosted due to the large magnetic pressure near the jet base.

We take a simplified treatment assuming that the corona photons are reflected by a photosphere of a single electron-scattering optical depth as seen by the corona. Since the Fe line is produced within the first few optical depths (Matt et al. 1993), we take a value between 1 and 3 for the optical depth of the reflection surface, which can be calculated as:

$$\tau_{\text{es}} = \int \kappa_{\text{es}} dl = \int 0.2(1 + \chi) \frac{\text{cm}^2}{\text{g}} dl = \int 0.34 \frac{\text{cm}^2}{\text{g}} dl, \quad (2)$$

where κ_{es} is the Thomson electron scattering opacity and $\chi = 0.7$ corresponds to the mass fraction of hydrogen with solar abundances. Here, only Newtonian calculations are used for the optical depth without considering the GR light-bending effect. We show the $\tau = 1$ and $\tau = 3$ photosphere surfaces in Fig. 1, clearly indicating that the reflection surface lies mostly in the optically-thick winds with large outflow velocities ($v_r > 0.1c$). Also, the reflection surface has a narrow half opening angle between $10 - 15^\circ$, which means the optically thick disk and wind will obscure the X-ray emission when viewed from side, so the corona and its reflection emission can only be seen by an observer looking directly down the narrow funnel.

Next, we investigate the motion of the reflection surface. As shown in Fig. 2a, the photosphere is first embedded within the inflow region of the accretion disk, but beyond $\rho \approx 6 R_g$ (ρ is the cylindrical distance) it is embedded within the outflow region of the winds. Along the photosphere v_r increases and then saturates towards a terminal speed of $v_r \approx 0.4 - 0.5 c$. The photosphere is rotating at sub-Keplerian velocity, and the radial velocity dominates over the rotational velocity after $\rho \approx 10 R_g$. Therefore, we should expect the X-ray reflection spectrum to be dominated by the radial motion of the winds, instead of the Keplerian motion of the disk as in the case of the standard model. The radial velocity of the photosphere of $\tau = 3$ has been fitted (within 5% deviation

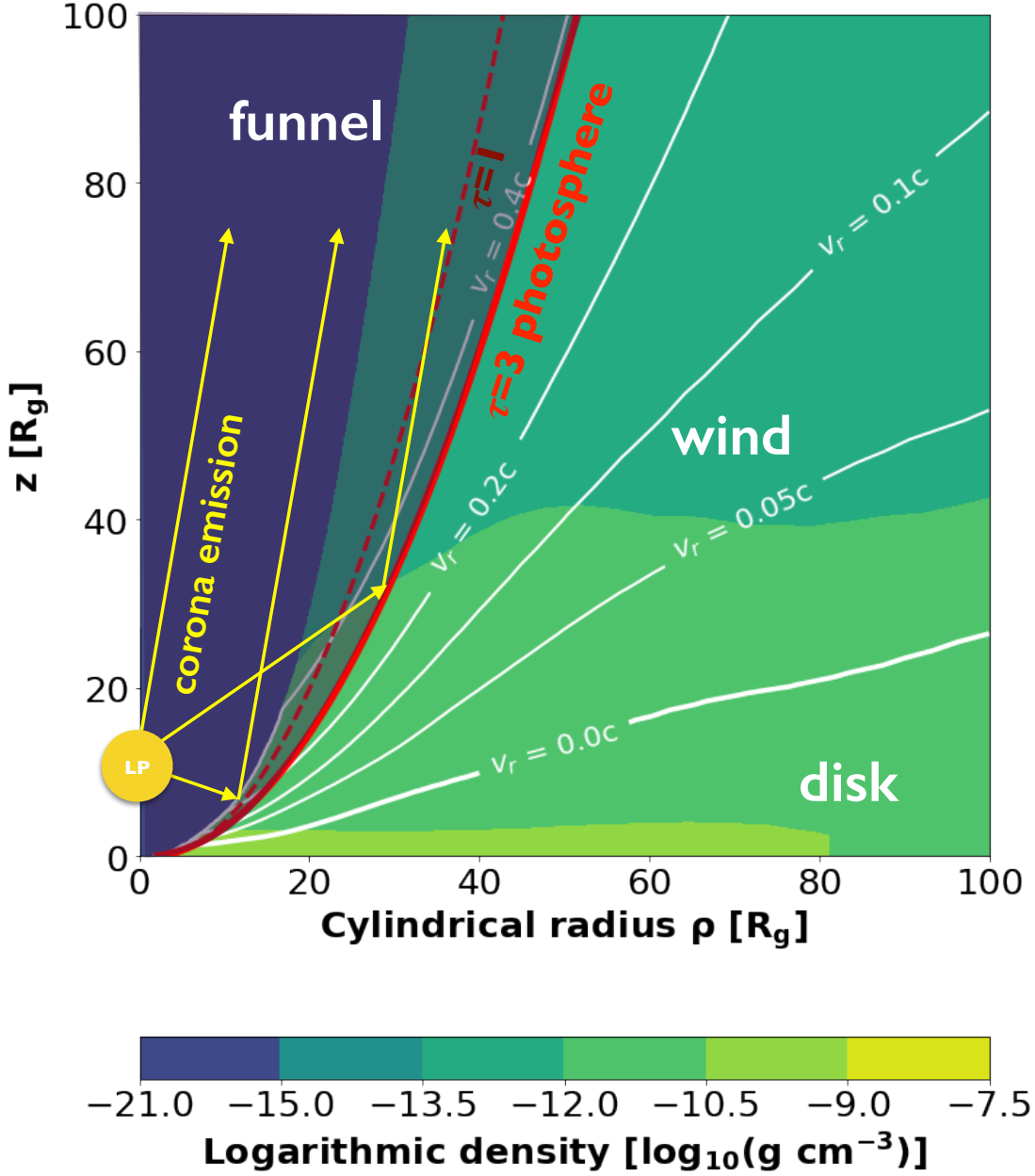


Figure 1. The geometry of the disk, winds, corona and its reflection surface for the simulated super-Eddington disk. The density of the disk and winds are shown by the background color in \log_{10} of cgs units [g cm^{-3}]. Here, the x and y axis are the cylindrical radius (ρ) and the vertical height (z). We have illustrated the jet (with $\beta < 1$) as the dark blue region around the pole. The white lines are the contours of constant radial velocity of the wind, which shows that wind moves slower at larger inclination. An optically-thin funnel (the shaded region) is located around the pole, and it is surrounded by the optically-thick wind. The yellow circle represents the (artificially placed and size-exaggerated) lamppost corona, which is located at a height of $10 R_g$ above the BH. The thick red line and thin dashed red line are respectively the electron-scattering photosphere of $\tau = 3$ and $\tau = 1$ integrated from the corona, and it represents the reflection surface. An observer looking down the funnel can see the direct emission from the corona, as well as the corona emission reflected by the funnel (including the Fe $K\alpha$ fluorescent lines).

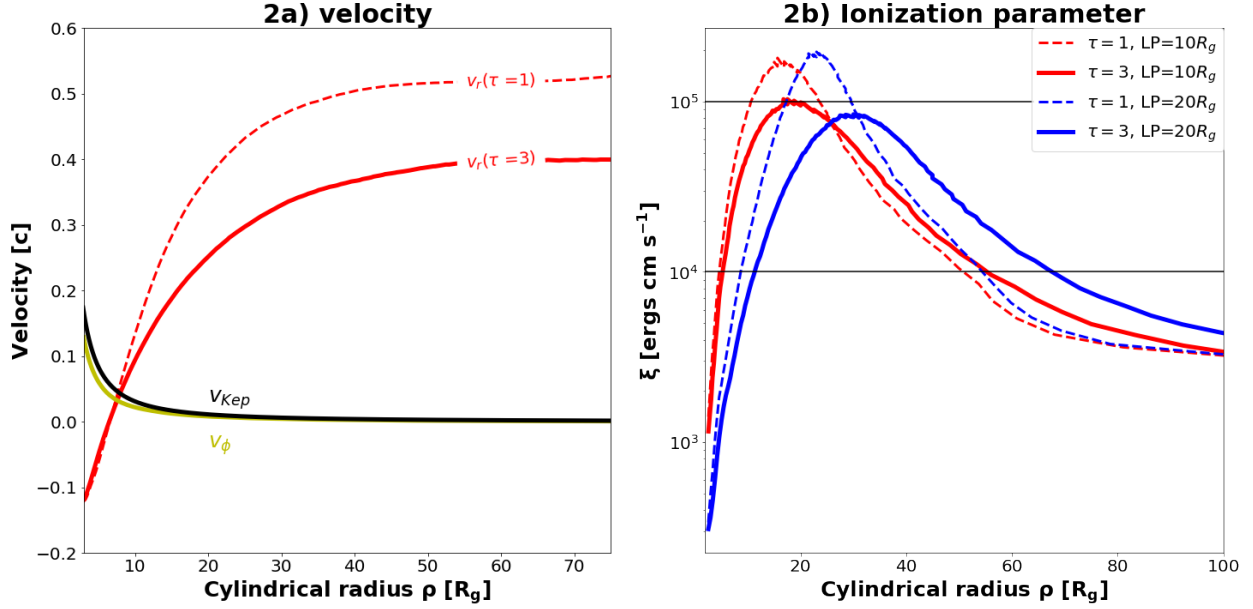


Figure 2. 2a. The radial and rotational velocity of the reflection surface. We convert the GR 4-velocity of the gas of the simulated accretion flow to the equivalent Newtonian 3-velocity. The red curve is the radial velocity of the photosphere with $\tau = 3$ and the thin dashed curve is that for the $\tau = 1$ photosphere. The rotational velocities of the two photospheres lay almost on top of each other (yellow curve). As a comparison, we have illustrated the Keplerian rotational velocity (black curve) alongside the rotational velocity, and show that the rotation of the thick disk/wind is sub-Keplerian. The motion in the polar direction is negligible and have therefore not been illustrated. Along this reflection surface, it can be seen that the wind starts to accelerate and eventually saturates at a terminal velocity of $v_r \approx 0.4-0.5 c$. The outward radial motion of the wind starts to dominate over the rotation beyond $\rho \approx 10 R_g$. Therefore, the Fe reflection spectrum is primary determined by the radial motion of the winds instead of the Keplerian motion as in the case of a thin disk. **2b. The ionization level of the reflection surface.** We show the ionization parameter in cgs units [ergs cm s^{-1}] along the photosphere as a function of the cylindrical distance. We show that the ionization level is not very sensitive to the choice of corona height or photosphere optical depth. We assume that the corona hard X-ray luminosity is $L_x = 0.1 L_{Edd}$. The ionization level is much higher compared to a thin disk case ($\xi \lesssim 1000$ erg cm s^{-1} from observational constraints) and therefore the production of hot Fe lines is favored. The two horizontal black lines mark the range of the ionization parameter where the hot Fe $K\alpha$ fluorescent line with rest-frame energy of 6.97 keV is likely produced.

in the wind region) with the following equation:

$$\frac{v_r}{c} = 0.5 - \frac{6.2 R_g}{6 R_g + \rho}. \quad (3)$$

The last crucial parameter investigated is the ionization level. The ionization parameter (ξ) depends on the density of the reflection surface and the hard X-ray irradiation flux, and it is calculated as (Reynolds & Begelman 1997):

$$\xi(r) = \frac{4\pi F_x}{n(r)}, \quad (4)$$

where $n(r)$ is the gas number density found from the simulated disk structure and F_x is the irradiating corona flux crossing the reflection surface. Using the Newtonian irradiation profile, the irradiating flux can be expressed analytically as:

$$F_x = \frac{L_x \cos(\psi)}{4\pi R_{LP}^2} = \frac{\eta_x L_{Edd} \cos(\psi)}{4\pi R_{LP}^2}, \quad (5)$$

where L_x is the luminosity of hard X-ray corona photons that can ionize Fe and $\eta_x = L_x/L_{Edd}$. Here, R_{LP} is the distance from the lamppost corona to the the gas element on the reflection surface, and ψ is the angle the vector from the corona to the reflection surface produces with the normal vector of the reflection surface. The ionization level will dictate whether Fe $K\alpha$ fluorescent lines can be produced, and if so whether a higher or lower ionization line (e.g., 6.4, 6.7 or 6.97 keV) can be seen (Ross et al. 1999; Ballantyne & Ramirez-Ruiz 2001). Since the corona production in super-Eddington accretion has not been systematically studied, we adopt $\eta_x = 0.1$ which is conventionally used for thin disk corona models. As illustrated in Fig. 2b, the ionization level is several orders of magnitudes higher than that of the theoretical thin disk (e.g., $\xi \lesssim 100$ erg cm s^{-1} outside the ISCO in Reynolds

& Begelman 1997). This is mainly because the density of the gas in the wind is much more dilute than that in a thin disk. It is interesting to notice that independent of initial configuration (τ -surface and lamppost height h_{LP}) of the reflection surface, the ionization level lies between 10^4 and 10^5 ergs cm s $^{-1}$. This ionization interval strongly favors the production of the hot and warm Fe K α lines with rest-frame energies of 6.97 and 6.7 keV, instead of the cold 6.4 keV Fe line seen from thin disks (Ballantyne & Ramirez-Ruiz 2001).

3. LINE PROFILE

In this section, we study how an initial Fe K α line emitted at a single energy in the co-moving frame of the emitting gas appears skewed and broadened due to the relative motion and different gravitational potentials between the emitting gas and the observer. This is calculated under a general relativistic framework. In Section 3.1, we first present a brief summary of the theory and our method for GR ray-tracing. In Section 3.2, we present the calculated Fe K α emission line profile, where we also investigate how robust the emission line profile is when changing the following physical parameters: the viewing angle, the choice of the optical depth for the reflection surface and the height of the irradiating lamppost.

3.1. Methodology for GR Ray-Tracing

When photons are emitted by gas in one frame and observed in another frame, the intensity shift of the photons between the two frames can be calculated using the Louivilles Theorem, which states that the photon phase-space density I_ν/ν^3 is conserved along the ray (Cunningham 1975). Here I_ν is the specific intensity at frequency ν , and we denote $I_{\nu_o}^{\text{obs}}$ to be the observed specific intensity at the observed frequency ν_o and $I_{\nu_e}^{\text{emit}}$ to be the emitted specific intensity at the emitted frequency ν_e . Thus we have:

$$I_{\nu_o}^{\text{obs}} = I_{\nu_e}^{\text{emit}} (\nu_o/\nu_e)^3 = g^3 I_{\nu_e}^{\text{emit}}. \quad (6)$$

Here, g is the energy shift (or the redshift) from the emitted photon to the observed photon, and it is defined by:

$$g \equiv \frac{\nu_o}{\nu_e} = \frac{E_{\text{obs}}}{E_{\text{emit}}}, \quad (7)$$

where E is the energy of the photon. Therefore, we can calculate the total intensity integrated over all frequencies by:

$$I^{\text{obs}} = \int I_{\nu_o}^{\text{obs}} d\nu_o \propto \int I_{\nu_e}^{\text{emit}} g^3 d\nu_o = \int I_{\nu_e}^{\text{emit}} g^3 d(g \nu_e) \propto g^4 I^{\text{emit}}. \quad (8)$$

We point out that for faraway sources, the observed flux and intensity are proportional to each other. The reason for this is that the specific flux at the observed frequency ν_o ($F_{\nu_o}^{\text{obs}}$) is the observed specific intensities $I_{\nu_o}^{\text{obs}}$ integrated across the solid angle of the emitting surface as seen by the observer. Therefore, we have:

$$F_{\nu_o}^{\text{obs}} = \int_{\text{source}} I_{\nu_o}^{\text{obs}} \cos(\theta_i) d\Omega \sim I_{\nu_o}^{\text{obs}} \Omega \propto I_{\nu_o}^{\text{obs}}. \quad (9)$$

Here, Ω is the solid angle of the reflection surface as seen by the the far away observer, and θ_i is the angle between the direction of the BH and incoming rays from the reflection surface, and since the observer is assumed to be far away, then $\cos(\theta_i) \sim 1$. Therefore, the total flux goes like $F \propto g^4$ as well.

We employ a GR ray-tracing code (Dai 2012, modified from Fuerst & Wu 2004) to calculate the photon trajectory from the emitting gas to a faraway stationary observer. The code uses the Boyer-Lindquist spherical coordinate system to describe the space-time around a Kerr black hole with the line element (in geometric units $G = M = c = 1$):

$$ds^2 = -\left(1 - \frac{2r}{\Sigma}\right) dt^2 - \frac{4ar \sin^2\theta}{\Sigma} dt d\phi + \frac{\Sigma}{\Delta} dr^2 + \Sigma d\theta^2 + \left(r^2 + a^2 + \frac{2a^2 r \sin^2\theta}{\Sigma}\right) \sin^2\theta d\phi^2, \quad (10)$$

where (t, r, θ, ϕ) is the Boyer-Lindquist spherical coordinates and $\Delta = r^2 - 2r + a^2$ and $\Sigma = r^2 + a^2 \cos^2\theta$. In this code, we calculate the geodesic of particles by evolving the six variables $t, r, \theta, \phi, p_r, p_\theta$ using the following equations:

$$\begin{aligned}
p_t &= -E & \dot{t} &= E + \frac{2r(r^2 + a^2)E - 2aL}{\Sigma\Delta} \\
p_r &= \frac{\Sigma}{\Delta} \dot{r} & \dot{p}_r &= \frac{(r-1)((r^2 + a^2)H - \kappa) + rH\Delta + 2r(r^2 + a^2)E^2 - 2aEL}{\Sigma\Delta} - \frac{2p_r^2(r-1)}{\Sigma} \\
p_\theta &= \Sigma \dot{\theta} & \dot{p}_\theta &= \frac{\sin\theta \cos\theta}{\Sigma} \left(\frac{L^2}{\sin^4\theta} - a^2(E^2 + H) \right) \\
p_\phi &= L & \dot{\phi} &= \frac{2arE + (\Sigma - 2r)L/\sin^2\theta}{\Sigma\Delta}
\end{aligned} \tag{11}$$

Here p_t and p_ϕ are constants of motion representing the conservation of energy (E) and angular momentum around the spin axis (L). Furthermore, we have two additional constants: H is the Hamiltonian (which is 0 for photons and -1 for massive test particles) and $\kappa = Q + L^2 + a^2(E^2 + H)$, where Q is Carter's constant ($Q = p_\theta^2 - a^2 E \cos^2\theta + L^2 \cot^2\theta$).

Evolving these six variables enables one to calculate the photon energy shift g from the frame of the emitting gas to the faraway observer as:

$$g = \frac{E_{\text{obs}}}{E_{\text{emit}}} = \frac{(p_\mu u^\mu)_{\text{obs}}}{(p_\mu u^\mu)_{\text{emit}}} = \frac{-E}{(p_\mu u^\mu)_{\text{emit}}}. \tag{12}$$

Here, the four velocity for a faraway stationary observer is $u^t = (1 - 2r/\Sigma)^{-1} \sim 1$, and u^μ_{emit} is the 4-velocity of the emitting gas along the reflection surface. For the super-Eddington disk, the 4-velocity of the gas element along the chosen photosphere is obtained directly from the GRRMHD simulation. For a thin disk, the reflection surface lies in the equatorial plane and is orbiting with prograde Keplerian 4-velocity (Bardeen et al. 1972):

$$\tilde{u}_{\text{gas}} = u^t(1, 0, 0, \Omega), \quad \text{where } \Omega = (a + \rho^{3/2})^{-1}, \quad \text{and } u^t = \frac{a + \rho^{3/2}}{\sqrt{\rho^3 - 3\rho^2 + 2a\rho^{3/2}}}. \tag{13}$$

Also, we only include emission from the disk region extending from the ISCO to $100 R_g$.

We also assume that the emitted fluorescent line intensity scales with the corona irradiation flux crossing the reflection surface (see Eq. 5). Therefore, the observed Fe $K\alpha$ line intensity can be calculated using the following equation:

$$I^{\text{obs}} = I^{\text{emit}} g^4 \propto g^4 \frac{\cos(\psi)}{R_{\text{LP}}^2}. \tag{14}$$

In the ray-tracing code, we use the standard fourth order Runge-Kutta integrator to evolve these equations together with adaptive step sizes, so the curved trajectories close to the BH can be numerically resolved. We also adopt the standard procedure to start from an image plane placed at $r = 1000 R_g$ and trace the photons backwards in time to the disk to save computing power.

3.2. Fe $K\alpha$ Reflection Spectrum From Super-Eddington Accretion Flow

In this section, we will present the calculated Fe $K\alpha$ line profile from the super-Eddington accretion disk, which is illustrated in Section 2, using the methods described in Section 3.1. We will show that the geometry of the reflection surface and the wind-launching physics are the first-order factors responsible for making the Fe line profile of super-Eddington accretors fundamentally different from the thin disk case. While simulations of super-Eddington accretion disks with different BH masses and spins or accretion rates have shown that the exact wind profile can depend on these parameters (McKinney et al. 2015; Sądowski & Narayan 2016; Jiang et al. 2017), which will affect the theoretical Fe line profile, they have also shown that the basic structure of the accretion flow stays the same and the wind speeds in the funnel region are similar to the first order. Therefore, the basic corona irradiation picture as illustrated in Fig. 1 should apply for generic super-Eddington systems. In this work, we only calculate the Fe reflection spectrum from a single simulated super-Eddington disk structure (Dai et al. 2018) in order to highlight its morphological difference to the standard Fe line spectrum of thin disks, since the exploration on how the exact funnel geometry or wind speed depends on various physical parameters goes beyond the scope of this short letter. Here, we will also check whether the first-order results stay robust against changes in the choice of the optical depth of the reflection surface τ and the height of the lamppost corona h_{LP} , and whether they sensitively depend on the inclination angle of the observer i .

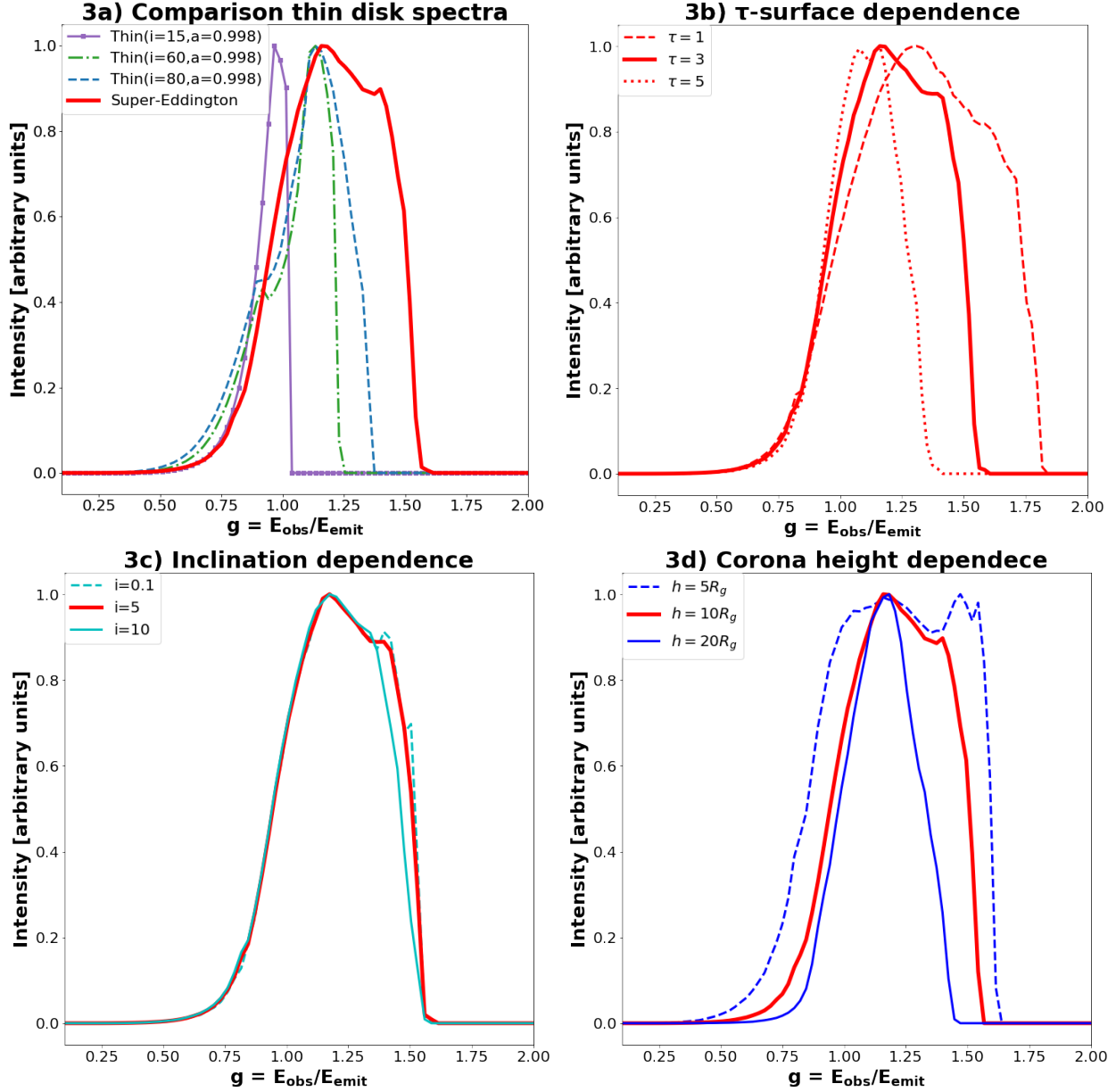


Figure 3. The intensity of fluorescent Fe $K\alpha$ line profiles from the simulated super-Eddington disk with different τ -surfaces, inclination angles and corona heights, and also in comparison with thin disk line profiles. The thick red line in all panels represent the fiducial case using $\tau = 3$, $h_{LP} = 10 R_g$ and $i = 5^\circ$. All the line profiles are scaled to have a maximum at 1. **3a. Comparison between the Fe line from the super-Eddington disk and thin disks (thin lines).** All the thin disks have spin parameter of $a = 0.998$. It can easily be seen that the Fe line of the thick disk is more blueshifted due to the large outflow speed of the winds. **3b. Dependence on the choice of the τ -surface.** We fix the corona height at $10 R_g$ and the inclination at 5° , but vary the optical-depth (τ) of the reflection surface. With increasing τ value, the funnel is wider with a lower wind terminal velocity, which reduce the blueshift and the width of the Fe line produced. **3c. Dependence on the viewing angle from the pole.** Here, we fix $h_{LP} = 10 R_g$ and $\tau = 3$ and vary the viewing angle to the observer. Note, the half opening angle of the funnel is very narrow ($i \sim 10 - 15^\circ$), so in order to observe the reflected Fe line, then the observer needs to look directly down the funnel, and hence there is not much freedom for varying i . Therefore, the Fe line profiles are almost independent of i as long we are observing down the funnel. **3d. Dependence on the height of the compact corona.** We only vary h_{LP} and keep everything else the same as in the fiducial case. A lower corona height gives more weight to the irradiation from the inner disk and therefore induces more gravitational redshift. It also produces a more blueshift line profile since the terminal velocity is higher due to the funnel, as seen by the corona, is narrower when lowering the corona height. Therefore, the width of the Fe line is correlated with the corona height.

Our fiducial configuration for the Fe line profile of the super-Eddington accretor is obtained using the following parameters: $\tau = 3$ (following [Matt et al. 1993](#)), $h_{LP} = 10 R_g$ and $i = 5^\circ$ (from the pole), and it is shown in all panels of [Fig. 3](#) as the red thick-line spectra. We first plot this line profile together with a few representative Fe line profiles of thin disks in [Fig. 3a](#). Consistent with previous studies ([Reynolds & Begelman 1997](#); [Dabrowski et al. 1997](#); [Reynolds et al. 1999](#)), the thin disk Fe line profile has a strong viewing-angle dependence, and it is always skewed to the right due to an extended red wing, which is caused by gravitational redshift. Only when a thin disk is viewed almost edge-on, one can observe a large blueshifted component (with $g = E_{obs}/E_{emit} > 1$) from the Doppler motion of the inner disk. However, for the almost face-on super-Eddington disk case, one can see that the Fe line is very strongly blueshifted because the reflecting gas elements are in the fast winds, which are moving towards the observer, who is looking down the funnel. We will discuss more details of these differences in [Section 4](#).

Second, we investigate the dependence on the choice of the photosphere. As shown in [Fig. 3b](#), the Fe line spectra produced from different τ surfaces have similar line shapes, while the peak of the Fe line profile is more blueshifted in the case of smaller τ values. The reason for this is that the photosphere with smaller τ values lies closer to the pole (see [Fig. 1](#)) where the wind moves faster. Also, the $\tau = 1$ Fe line profile has a broader width due to the larger velocity variance of the wind speed along this photosphere. Here, we have simplified the reflection geometry to be a reflection surface of a single τ value, although the real scenario can be a combination of multiple scatterings of photons in the optically-thick winds at different optical depths. It is hard to get an accurate Fe line profile without doing a detailed radiative transfer simulation. However, the similarity between the line shapes across different τ surfaces indicates that the Fe line profile obtained this way is a good approximation.

Next, we show in [Fig. 3c](#) that the observed Fe line profile has a very weak dependence on the inclination angle of the observer as long the observer is looking directly down the funnel. However, observing the corona and its reflected emission does depend heavily on the viewing angle because when it is observed at other directions than looking directly down the narrow funnel (with an half opening angle of $10 - 15^\circ$), then the optically thick disk and wind will obscure the emission. Therefore, only a small variation in the viewing angles of an observer, which can detect the reflected spectrum, is possible, so one would not expect any large differences in the Fe line profiles. The viewing-angle dependence is further weakened since the radial motion of the wind dominates over its rotation and the blueshift caused by the latter is negligible.

Lastly, we investigate the corona height dependence of the line profile. Since the photosphere is calculated from the corona, its geometry, velocity and irradiation profile all depend on the corona location. In the thin disk case, a compact corona at $h_{LP} = \text{few } R_g$ usually fits the observations (see [Reis & Miller 2013](#)). For a super-Eddington disk, we assume that the corona is located at a similar height, and here we show the Fe line profiles of three different corona heights of 5, 10, and 20 R_g in [Fig. 3d](#). The photosphere calculated from a higher corona height has a larger half opening angle at large radii. Therefore, the corresponding Fe line profile is less blueshifted and narrower. It can further be seen that lowering the corona height to 5 R_g will greatly broaden the red wing of the line since the irradiating flux on the photosphere close to the BH, where the gravitational redshift is the strongest, will be higher. This effect will become even more dramatic if the irradiation profile is calculated using general relativity with light bending effects.

4. USING THE IRON LINE PROFILE TO IDENTIFY SUPER-EDDINGTON SOURCES

In the previous section, we have compared a few representative Fe line profiles of thin disks to those from a super-Eddington disk. In this section, we will further do a systematic comparison, and show that the Fe line signatures between the two types of disks are morphologically different.

First, as we have shown in [Section 2](#), the reflection surface in the case of a super-Eddington disk has a much higher ionization level, which will likely produce hot Fe K α lines such as the 6.97 keV rest-frame energy line instead of the cold 6.4 keV line. Apart from this, the shape of the line profiles and the temporal signatures from the two types of disks are also distinguishable, and it is caused by the different geometry in the reflection surfaces together with relativistic effects. Therefore, we show the Fe line spectra as a function of the redshift g instead of the observed energy to better illustrate this.

Second, photons emitted from various radii on the reflection surface from the two types of disks contribute very differently to the line spectra. For thin disks in [Fig. 4a](#), [4b](#) and [4c](#), one can see that more than half of the line flux is contributed by photons emitted from within $\rho = 25 R_g$ of the disk because the irradiation profile drops quickly faraway from the BH. As a comparison, for the super-Eddington disk case ([Fig. 4d](#)), there is more weight to photons emitted at $\rho \approx 25 - 50 R_g$ when compared to the thin disk case. This is due to that the observed flux drops more slowly at large distances from the BH because of the curvature of the reflection surface and the large energy-shift of the reflected photons in the fast moving winds. Furthermore, for the thin disks with moderate-to-large viewing angles ([Fig. 4b](#) and [4c](#)), each annulus of the disk produces a double-peak line feature, and the most dramatic redshift and blueshift are produced from the innermost part of the disk ($\rho < 10 R_g$), where the rotation speed is the fastest and the relativistic effects are the strongest. For the face-on thin disk, all parts of the disk only produce redshifted photons.

However, for the face-on super-Eddington case, the photons emitted from the innermost disk (where the wind velocity is small) only contributes to the red wing, and the photons emitted at larger radii increases slowly in the observed blueshifted energies due to the wind acceleration. Therefore, the case between high inclination thin disks and super-Eddington accretors should be distinguishable by conducting a careful temporal study on the response at different energy ranges of the line spectra to changes in the corona continuum emission.

Last, we check if the Fe line profile of the super-Eddington disk is generically more blueshifted and symmetric with respect to the line center when compared to the thin disk cases. For this, we have generated a phase-space plot in Fig. 5, where we compare the Fe line features from the super-Eddington disk with those from a sample of 1500 thin disks. The thin disk sample is created by randomly sampling from a uniform distribution of BH spin between a Schwarzschild BH ($a = 0$) to a maximally rotating astrophysical BH ($a = 0.998$) (Thorne 1974), as well as random sampling from a uniform distribution of solid angles with inclination angles up to 80° (beyond which the disk is usually obscured by itself or some torus at large radius). We quantify the blueshift (\tilde{F}) of the Fe line as the percentage of the total integrated line intensity above $g = 1$. Additionally, the symmetry with respect to the line center (\tilde{w}) is defined as the ratio between the width of the blue wing to the width of the red wing. Here, the line center is defined as the place from where each side has half of the integrated line flux. The blue wing refers to the side bluer than the line center containing 50–95% of the line flux, and the red wing is the redder side containing 5–50% of the line flux. Both these parameters can be visualized in the two panels on the left-hand side in Fig. 5. The main panel on the right-hand side shows the values of these parameters calculated for the thin disk cases and the super-Eddington disk case. It can be seen that the Fe line profiles from the super-Eddington case have much larger blueshifts than all of the thin disk cases. Actually, for thin disks, the line can be either redshifted or blueshifted, mainly depending on the inclination angle of the observer. Here, we acknowledge that our Newtonian emissivity profile (Eq. 5) does not include light bending towards the BH, thus giving less weight to the innermost disk region. Therefore, the difference brought by the spin is underestimated. In Fig. 5, we can also see that the Fe line profiles of the super-Eddington disk are significantly more symmetric (with width ratio $\tilde{w} \approx 1$) when compared to the thin disk cases. All the Fe lines produced by thin disks are skewed to the blue wing because of relativistic beaming effects and gravitational redshift. Therefore, the shape of Fe line of a thin disk is generally less symmetric than the super-Eddington case. For the super-Eddington case, we have tested the robustness against the choice of lamppost height ($h_{LP} = 5 - 20 R_g$) and optical depth of the reflection surface ($\tau = 1 - 5$), and it can be seen that the first order results are robust.

In summary, we have demonstrated that the super-Eddington disk Fe line should occupy a significantly different parameter space when analyzing the rest-frame energy, blueshift and the symmetry of the lines profile. When combining these factors, and aided with temporal lag analysis, one can distinguish super-Eddington accreting systems from standard thin disk systems.

5. DISCUSSION AND FUTURE WORK

In this letter, we have presented a first theoretical investigation of the Fe $K\alpha$ fluorescent line profile produced from a lamppost corona irradiating a simulated super-Eddington accretion disk structure. The main results are summarized below.

- The reflection surface, where the Fe $K\alpha$ fluorescent lines are produced, can be represented by the wall of an optically thin funnel embedded in the optically thick winds. This is in contrast to the standard case where reflection happens at the surface of a (razor) thin disk.
- At large inclination angles, the optically-thick disk and wind, produced by super-Eddington accretion, will obscure the corona emission and its reflection spectrum. Therefore, the Fe $K\alpha$ lines can only be seen by observers looking at the system from a small range of inclination angles close to the pole, so observation of the reflected X-ray spectra should be accompanied with traces of jetted emission as well.
- The ionization level of the reflection surface is high, so the production of hot Fe $K\alpha$ lines with rest-frame energies of 6.97 or 6.7 keV are favored over the cold 6.4 keV Fe line.
- The Fe line profile is primarily determined by the geometry and the radial motion of the winds along the funnel wall instead of the Keplerian motion of the disk. The line spectra is mostly blueshifted. Also, photons emitted outside $10 R_g$ contribute more to the line flux due to the acceleration of the wind until large radii and the curvature of the reflection surface.
- The Fe line profile is robust against choosing different values of the optical depth to calculate the reflection surface, which indicates that the simple treatment of assuming all corona emission is reflected by a single surface is a good approximation of the realistic multiple-scattering scenario. The first-order features of the line profile also do not change with the height of the lamppost corona.

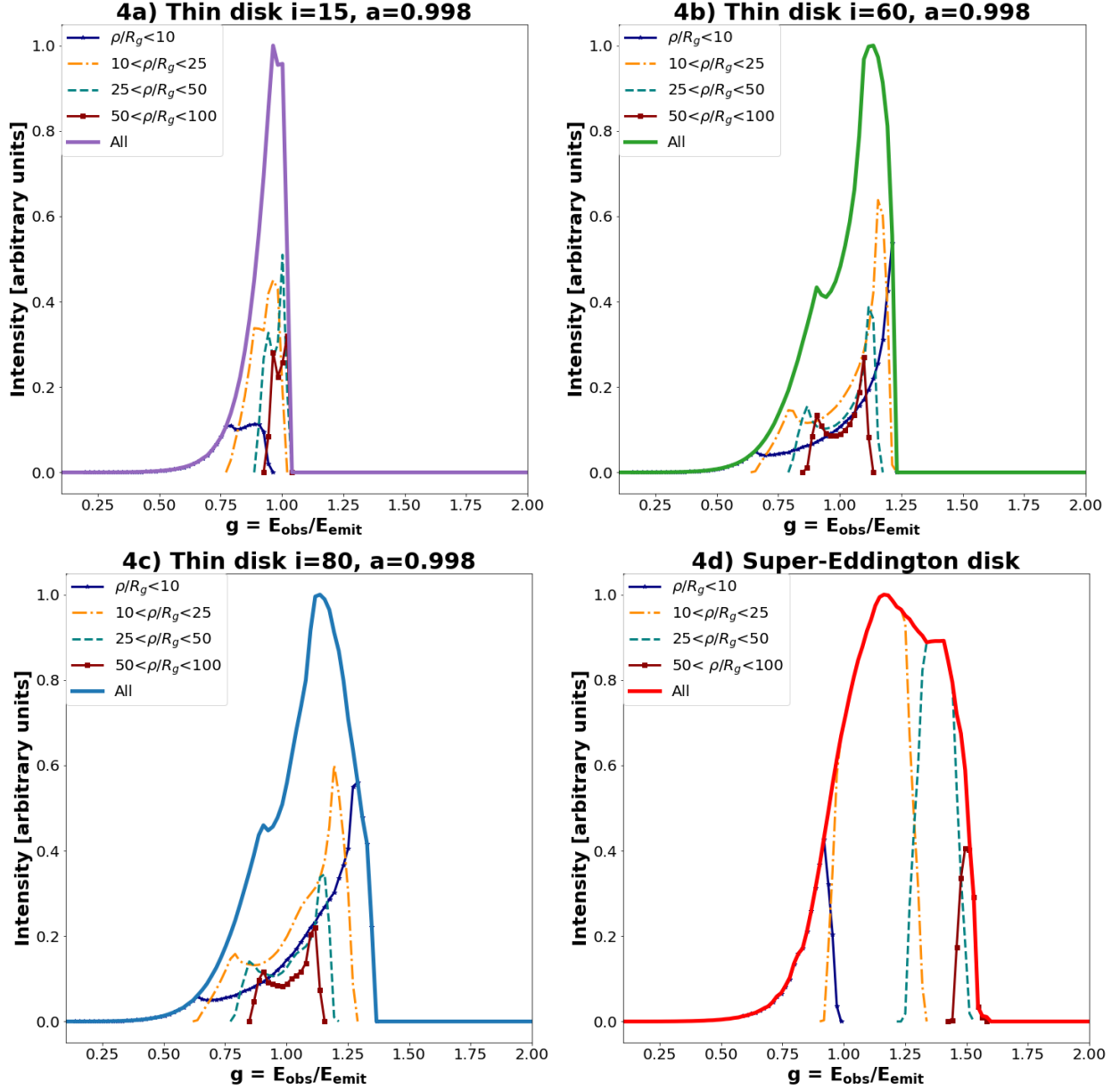


Figure 4. Decomposition of the Fe line profile based on the radii of emission. All panels show the contribution from each cylindrical radial bin (see their respective labels for interval) towards the total line profile given by the thick solid lines. All line profiles are scaled to have maximum at 1. **4a, 4b, 4c) Radial contribution towards the line profile for the thin accretion disk with spin $a = 0.998$ and respective inclination of $i = 15^\circ$, 60° or 80° .** For all three thin disk spectra, the contribution from within $\rho < 25 R_g$ dominates the total line flux since the irradiation profile favours the inner disk. Due to the vicinity of the BH and the large rotational velocity, the line spectra produced from this region is broadest with both a strong gravitational redshift and Doppler shift (when viewed from side). **4d) Radial contribution towards the line profile for the super-Eddington accretion disk.** It can be seen that the innermost region close to the BH horizon contributes solely to the red wing of the line profile due to the gravitational redshift and low wind outflows. It can further be seen that the bluest part of the line profile comes from the largest distances, since the wind speed first accelerates and eventually saturates towards a terminal velocity. Also the contribution from $\rho > 25 R_g$ is significant compared to the thin disk due to the irradiation profile and Doppler boosting.

- By comparing the Fe $K\alpha$ line profile between the super-Eddington disk and thousands of thin disks sampled with random spin parameters and orientation, we have shown that the Fe reflection line profile from a super-Eddington disk is distinctively more blueshifted and symmetric with respect to the line center. This result is also robust against the choice of reflection surface or the lamppost height of the super-Eddington accretor.

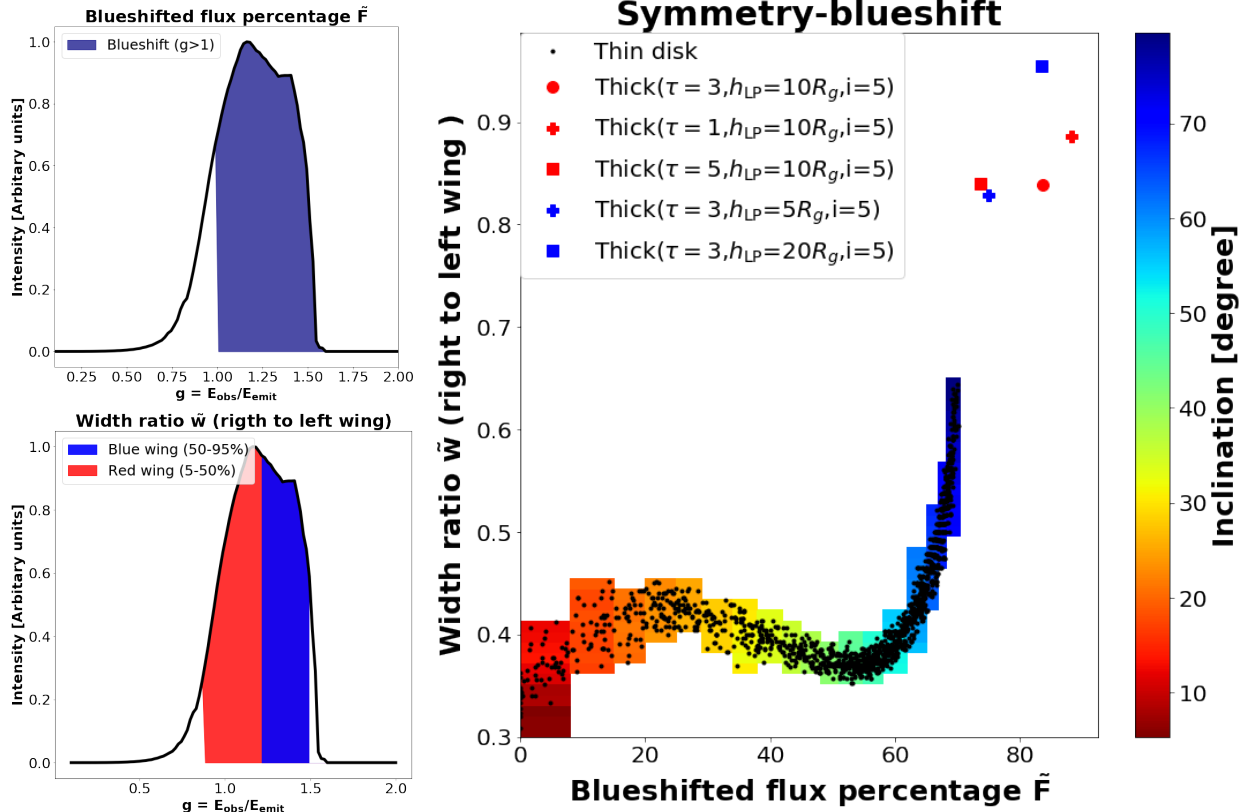


Figure 5. Phase-space diagram illustrating the morphological differences between the blueshift and the symmetry of Fe line profiles from both super-Eddington and thin disks. The two panels on the left-hand side illustrate how we calculate the two phase-space parameters; the blueshifted flux (\bar{F}) and the width ratio (\bar{w}). Here, \bar{F} is defined as the percentage of the total integrated Fe line flux, which lies above the rest-frame energy, and \bar{w} is the width ratio between the blue wing (where 50%-95% of the total line flux lies) to left wing (with 5%-50% of the total line flux). In the main panel on the right-hand side, we show the two parameters in a phase-space diagram for approximately 1500 thin disks, which are randomly sampled from a uniform distribution of spin parameters between 0 and 0.998 and solid angles up to an inclination angle of 80° . The thin disk data is marked by the black points in the phase space diagram, and the different configuration of the super-Eddington disks are marked by the large red/blue symbols. The color scheme in the background indicates the inclination angle between the thin disks and the observer (red – face on, blue – edge on). For thin disks, we find this blueshifted flux parameter (\bar{F}) has a strong correlation with the inclination angle (the dependence on the spin is weak since we currently use a Newtonian irradiation profile). Additionally, we find that the Fe lines from the super-Eddington disk are much more blueshifted than what is even possible for high inclination thin disks. Furthermore, the width ratio (\bar{w}), for thin disks, is always smaller than one since the line profiles are always skewed towards the blue side due to the gravitational redshift (which produces an extended red wing) and the relativistic boosting (which breaks the symmetry of the double-peak features). The Fe $K\alpha$ line profiles of the super-Eddington disk are much more symmetric because emissions from the inner disk has less weight due to the funnel geometry, and the large terminal wind speed greatly broadens the blue wing of the Fe line spectrum.

Actually, the strongly blueshifted hot Fe $K\alpha$ fluorescent line predicted here has been observed from a jetted TDE *Swift* J1644 (Kara et al. 2016). TDEs are believed to be super-Eddington accretors if the BH mass is smaller than a few $\times 10^7 M_\odot$ (Rees 1988; Evans & Kochanek 1989; Ramirez-Ruiz & Rosswog 2009; Guillochon & Ramirez-Ruiz 2013; Dai et al. 2015; Wu et al. 2018), and the existence of a relativistic jet in *Swift* J1644 (Burrows et al. 2011; Bloom et al. 2011; Berger et al. 2012; De Colle et al. 2012) further supports that a transient magnetized thick disk has been formed from the stellar debris (Tchekhovskoy et al. 2014). In Kara et al. (2016), the observed Fe line has an energy peaked at ~ 8 keV, which for an Fe $K\alpha$ emission line with a rest-frame energy of 6.97 keV corresponds to an energy-shift of $g = 1.15$ or an outflow velocity of $0.2-0.5 c$ depending on the half opening angle of the funnel and thus the lamppost height. Also, since we are looking directly along the jet in this system, it is likely that we are looking at the disk face on. This strongly disfavors the scenario of a standard thin disk because the Fe line should only be gravitationally redshifted from such inclination angles. Additionally, if we have corrected the Fe line profile of the super-Eddington accretor in Fig. 3 with the ionization level, then the over-ionized region close to the black hole will contribute less to the Fe line production. This will reduce the red wing and help explain the narrowness of the strongly blueshifted line from *Swift*

J1644. Actually, if we include general relativistic corrections to the emissivity profile, then the inner disk will become even more over-ionized due to the GR light-bending effect and gravitational blueshift from the corona to the disk. We will explore these effects in a future paper. Here, we do not attempt to fit the observed lines with our model because the parameters we used for the disk simulation may not be the same as in *Swift* J1644. Nonetheless, the similarity between the observed and simulated Fe K α line profiles demonstrates that it is promising to use such line profiles, as well as the time lag analysis between different energy ranges of the line with the continuum, to search for super-Eddington systems and study their disk geometry and wind-launching physics.

We aim at extending the fruitful study of X-ray reverberation on thin disk structures to also cover super-Eddington accretion disk geometries. In this letter, we have shown that the X-ray Fe fluorescent lines can be used to effectively distinguish super-Eddington systems from sub-Eddington systems. Future studies, such as calculating the irradiation profile in a rigorous GR setting, experimenting with different corona and disk geometries and tracing multiple scatterings of photons in the optically thick winds, can all improve our understanding on this topic. The study of X-ray reverberations on super-Eddington accretion flow can be used to constrain the funnel geometry and wind speed in TDEs, ULXs and super-Eddington Narrow-Line Seyfert 1 Galaxies, and it can help determine how the wind-launching depends on the Eddington ratio. Such studies can also shed more light on how quasars in the early universe provide kinetic feedback to their host galaxies.

We acknowledge helpful discussions with Roger Blandford, Cole Miller, Sandra Raimundo, Corbin Taylor, Marianne Vestergaard, Dan Wilkins, and Yajie Yuan. We are indebted to the David and Lucile Packard Foundation, the Heising-Simons Foundation and the Danish National Research Foundation (DNRF132) for support. Part of the simulations used in this paper were performed on the University of Copenhagen high-performance computing cluster funded by a grant from VILLUM FONDEN (project number 16599).

REFERENCES

- Abramowicz, M. A., Calvani, M., & Nobili, L. 1980, *ApJ*, 242, 772
- Alexander, K. D., Wieringa, M. H., Berger, E., Saxton, R. D., & Komossa, S. 2017, *ApJ*, 837, 153
- Balbus, S. A. & Hawley, J. F. 1991, *ApJ*, 376, 214
- Ballantyne, D. R. & Ramirez-Ruiz, E. 2001, *ApJ*, 559, L83
- Bardeen, J. M., Press, W. H., & Teukolsky, S. A. 1972, *ApJ*, 178, 347
- Begelman, M. C. 1978, *MNRAS*, 184, 53
- Berger, E., Zauderer, A., Pooley, G. G., et al. 2012, *ApJ*, 748, 36
- Blandford, R., Yuan, Y., Hoshino, M., & Sironi, L. 2017, *SSRv*, 207, 291
- Bloom, J. S., Giannios, D., Metzger, B. D., et al. 2011, *Science*, 333, 203
- Burrows, D. N., Kennea, J. A., Ghisellini, G., et al. 2011, *Nature*, 476, 421
- Cunningham, C. T. 1975, *ApJ*, 202, 788
- Dabrowski, Y., Fabian, A. C., Iwasawa, K., Lasenby, A. N., & Reynolds, C. S. 1997, arXiv e-prints, astro
- Dai, L. 2012, *Stanford Thesis*
- Dai, L., McKinney, J. C., & Miller, M. C. 2015, *ApJL*, 812, L39
- Dai, L., McKinney, J. C., Roth, N., Ramirez-Ruiz, E., & Miller, M. C. 2018, *ApJ*, 859, L20
- De Colle, F., Guillochon, J., Naiman, J., & Ramirez-Ruiz, E. 2012, *ApJ*, 760, 103
- Evans, C. R. & Kochanek, C. S. 1989, *ApJ*, 346, L13
- Fabian, A. C., Rees, M. J., Stella, L., & White, N. E. 1989, *MNRAS*, 238, 729
- Fuerst, S. V. & Wu, K. 2004, *A&A*, 424, 733
- Guillochon, J. & Ramirez-Ruiz, E. 2013, *ApJ*, 767, 25
- Jiang, Y.-F., Stone, J., & Davis, S. W. 2017, arXiv e-prints, arXiv:1709.02845
- Jiang, Y.-F., Stone, J. M., & Davis, S. W. 2014, *ApJ*, 796, 106
- Kara, E., Dai, L., Reynolds, C. S., & Kallman, T. 2018, *MNRAS*, 474, 3593
- Kara, E., Miller, J. M., Reynolds, C., & Dai, L. 2016, *Nature*, 535, 388
- Kara, E., Steiner, J. F., Fabian, A. C., et al. 2019, *Nature*, 565, 198
- Matt, G., Fabian, A. C., & Ross, R. R. 1993, *MNRAS*, 262, 179
- Matt, G., Perola, G. C., & Piro, L. 1991, *A&A*, 247, 25
- McKinney, J. C., Dai, L., & Avara, M. J. 2015, *MNRAS*, 454, L6
- McKinney, J. C., Tchekhovskoy, A., Sadowski, A., & Narayan, R. 2014, *MNRAS*, 441, 3177
- Novikov, I. D. & Thorne, K. S. 1973, in *Black Holes (Les Astres Occlus)*, 343
- Ohsuga, K., Mineshige, S., Mori, M., & Kato, Y. 2009, *Publications of the Astronomical Society of Japan*, 61, L7
- Pinto, C., Middleton, M. J., & Fabian, A. C. 2016, *Nature*, 533, 64
- Ramirez-Ruiz, E. & Rosswog, S. 2009, *ApJL*, 697, L77
- Rees, M. J. 1988, *Nature*, 333, 523
- Reis, R. C. & Miller, J. M. 2013, *ApJ*, 769, L7
- Reynolds, C. S. 2014, *SSRv*, 183, 277
- Reynolds, C. S. & Begelman, M. C. 1997, *ApJ*, 488, 109

- Reynolds, C. S., Young, A. J., Begelman, M. C., & Fabian, A. C. 1999, *ApJ*, 514, 164
- Ross, R. R., Fabian, A. C., & Young, A. J. 1999, *MNRAS*, 306, 461
- Schnittman, J. D., Krolik, J. H., & Noble, S. C. 2013, *ApJ*, 769, 156
- Shakura, N. I. & Sunyaev, R. A. 1973, *A&A*, 500, 33
- Sądowski, A. & Narayan, R. 2016, *MNRAS*, 456, 3929
- Sądowski, A., Narayan, R., McKinney, J. C., & Tchekhovskoy, A. 2014, *MNRAS*, 439, 503
- Taylor, C. & Reynolds, C. S. 2018, *ApJ*, 855, 120
- Tchekhovskoy, A., Metzger, B. D., Giannios, D., & Kelley, L. Z. 2014, *MNRAS*, 437, 2744
- Thorne, K. S. 1974, *ApJ*, 191, 507
- Wilkins, D. R. & Fabian, A. C. 2012, *MNRAS*, 424, 1284
- Wu, S., Coughlin, E. R., & Nixon, C. 2018, *MNRAS*, 478, 3016
- Wu, S.-M. & Wang, T.-G. 2007, *MNRAS*, 378, 841
- Yuan, Y., Blandford, R. D., & Wilkins, D. R. 2019, *MNRAS*, 484, 4920